Extended Isogeometric Analysis of Cracked Piezoelectric Materials in the Presence of Flexoelectricity

Unnikrishnan, Gokul Krishna; Sharma, Saurav; Pathak, Himanshu; Chauhan, Vishal Singh; Jain, Satish Chandra

DOI
10.1002/adts.202200846

Publication date
2023

Document Version
Final published version

Published in
Advanced Theory and Simulations

Citation (APA)
Unnikrishnan, G. K., Sharma, S., Pathak, H., Chauhan, V. S., & Jain, S. C. (2023). Extended Isogeometric Analysis of Cracked Piezoelectric Materials in the Presence of Flexoelectricity. *Advanced Theory and Simulations*, *6*(4), Article 2200846. https://doi.org/10.1002/adts.202200846

ADVANCED THEORY AND SIMULATIONS
www.advtheorysimul.com

Extended Isogeometric Analysis of Cracked Piezoelectric Materials in the Presence of Flexoelectricity

Gokul Krishna Unnikrishnan, Saurav Sharma, Himanshu Pathak, Vishal Singh Chauhan, and Satish Chandra Jain*

To accurately analyze the fracture behavior of piezoceramics at small length scales, flexoelectricity must be considered along with piezoelectricity. Due to its dependence on size, flexoelectricity predominates at the micro- and nano-length scales. Additionally, crack tips having the largest strain gradient state cause large flexoelectricity around them. Different approaches are employed in the past to model cracks computationally. However, extended isogeometric analysis (XIGA) is proven to be an accurate and efficient method. C^1 continuity requirements for modeling gradients in flexoelectricity are met by non-uniform rational B-splines (NURBS) basis functions used in XIGA. In this work, XIGA-based computational model is developed and implemented to study the fracture behavior of the piezoelectric-flexoelectric domain. An in-house MATLAB code is developed for the same. Several numerical examples are studied to ensure the efficacy and efficiency of the implemented model, and crack behavior is presented in the form of an electro-mechanical J-integral. The analysis is carried out to investigate how cracks behave for different flexoelectric coefficients under different electrical and mechanical loading combinations. J-integral is also analyzed against crack parameters such as crack orientation and length. It is observed that boundary loads and flexoelectric material constants significantly influence J-integral. Results also show a considerable amount of fracture toughening in the presence of flexoelectricity. The peak value of J-integral is found to be reduced with an increase in the flexoelectric coefficient. A significant reduction in J-integral, as much as 45%, is observed when the flexoelectric constant varied from 0.5 to 2 μCm^{-1}.

1. Introduction

Smart materials are extensively employed for fabricating sensors, actuators, and energy harvesters. These materials are known for their ability to react to external stimuli in a useful, reliable, and reproducible manner.[1,2] External stimuli can be mechanical, chemical, electrical, magnetic etc. Piezoelectric materials are widely used smart materials for sensing and actuation applications. They have been widely used in MEMS/NEMS devices as micro/nano-sensors, actuators, and energy harvesters.[3–5] The reversible coupling between mechanical deformation and electric potential makes piezoelectrics desirable for these applications. Piezoelectric behavior comes with a special requirement known as a non-centrosymmetric crystal structure. Also, for ferroelectric-piezoelectric material, piezoelectricity is shown only below Curie temperature.[6] Dielectrics also possess another electro-mechanical coupling phenomenon known as flexoelectricity. Flexoelectricity is defined as the effect of generating electric potential proportional to strain gradient and, in a reverse manner, mechanical strain from electric field gradients. Flexoelectricity does not require a non-centrosymmetric crystal structure, making it a more general property than piezoelectricity.[7] Due to its universal presence regardless of crystal structure, flexoelectricity has recently been getting lots of research attention from both theoreticians and experimentalists.[8–11] The flexoelectric effect in solids was first identified in 1957 by Mashkevich and Tolpygo.[12] The framework for defining flexoelectricity as a phenomenon was developed by Mindlin in 1968.[13] Researchers investigated flexoelectricity in sensing,[14] actuation,[15,16] and energy harvesting.[17–19] Since it is a gradient-dependent phenomenon and gradients increase with reducing length scale, its effect is high at micro and nano levels.[20] Even flexoelectricity competes with piezoelectricity in many nanotechnology applications.[9] So it is essential to incorporate flexoelectricity while designing micro and nano-level piezoelectric devices.[21]

Since flexoelectricity is prominent in places with higher strain gradients, holes, cracks, thin films, and inclusions are naturally targeted for their presence.[22–24] Stress fields are singular at crack tips, and the high value of stress reduces at a minimal distance resulting in high strain gradients around the tip. The high strain gradient will allow flexoelectricity to act and generate

G. K. Unnikrishnan, H. Pathak, V. S. Chauhan, S. C. Jain
School of Mechanical and Materials Engineering
Indian Institute of Technology
Mandi, Himachal Pradesh 175075, India
E-mail: d19001@students.iitmandi.ac.in

S. Sharma
Faculty of Mechanical
Maritime and Materials Engineering
Delft University of Technology
Mekelweg 2, CD Delft 2628, The Netherlands

The ORCID identification number(s) for the author(s) of this article can be found under https://doi.org/10.1002/adts.202200846

DOI: 10.1002/adts.202200846

electric potential proportional to it.[25] An earlier Investigation of flexoelectricity associated with cracks was carried out in ice by Petrenko et al.[26] and was given as the reason for polarization associated with cracks and dislocation in ice, a centrosymmetric crystal that does not possess piezoelectricity. The name "pseudo piezoelectricity" was given to the phenomenon then. In their 2015 study, Mao et al.[25] investigated flexoelectricity associated with defects and cracks. Some recent studies also found that flexoelectricity contributes to the healing and repairing of cracks in bones. Vasquez-Sancho et al.[27] quantified the flexoelectricity-induced electric fields around crack tips in bone minerals and concluded that they are sufficiently large for osteocyte apoptosis. Núñez-Toldrà et al.[28] conducted detailed cellular-level experiments focusing on the mechanism of the healing process and concluded that flexoelectricity triggers an apoptotic response and induces bone rebuilding.

Crack behavior depends only on mechanical boundary loads for structures made with materials having prominent mechanical characteristics. In the case of fracture mechanics of piezoelectric materials, the crack behavior is influenced by both mechanical and electrical boundary loading, such as traction and electric charge density at the boundary. While designing using piezoelectric materials, their low strength and brittle nature must be considered to prevent fracture against electrical and mechanical loading.[29,30] Fracture mechanics of piezoelectric materials has been widely investigated in the past.[31] Many researchers have used the finite element method (FEM)[32] and the extended finite element method (XFEM) to implement fracture studies on piezoelectric materials under electro-mechanical and thermal loading.[33–38] In some of the recent contributions, Zhu et al. conducted dynamic fracture analysis of inhomogeneous piezoelectric materials[39] and piezoelectric composites.[40] Compared with piezoelectricity, fracture mechanics of domains with flexoelectricity is still a less explored area.[24,25] Gradients must be considered when modeling flexoelectricity, and XFEM's linear Lagrange-based finite elements cannot be employed.[41] Isogeometric analysis (IGA) using NURBS as smooth basis functions can interpolate gradients and higher-order fields. A MATLAB-based implementation of IGA for various problems was developed by Nguyen et al.[42] Their computational framework covers linear elastic fracture mechanics and structural mechanics problems.

Different computational models have been developed to model flexoelectricity in the past.[41,43] In one of the early works, Abdollahi et al.[20] implemented a numerical model using the meshfree method for analysis of the flexoelectric effect in beams and truncated pyramids. IGA, capable of modeling gradients, was applied to capture flexoelectricity in many works.[21,44–48] Yvonnet et al.[49] used Argyris elements in their study, which provides C^1 continuity to the displacement field. Similar to XFEM was developed for solving fracture problems, XIGA was developed to solve crack problems using isogeometric analysis.[50] Partition of unity character of NURBS allows adding enrichment functions to approximations in knot span in a similar way as that of XFEM. XIGA is similar to XFEM, and the major difference is that the Lagrange polynomial basis and derivatives were straightforward to implement, while a separate algorithm has to be implemented for NURBS derivatives. XIGA has been applied to piezoelectric problems in some previous works,[34,51] and J-integral was employed to study the behavior of the crack.[52,53] Since most ferroelectric materials are brittle, we can ignore crack tip plasticity in them, and the J-integral developed would equal the energy release rate.[54] Sladek et al.[55] developed an FE-based formulation for higher-order piezoelectric fracture problems. The length scale parameters were used for incorporating gradients into the coupling, and the model was implemented using COMSOL.[56] In another contribution, Abdollahi et al.[57] investigated cracked domains using meshless method at different length scales with piezoelectricity and flexoelectricity. The energy release rate was used for studying the crack behavior and noted a significant amount of fracture toughening and asymmetry at specific length scales.

The literature review found that different computational and analytical models have been used to model cracks in flexoelectric domains, such as meshless methods and FEM with adaptive meshing. Although, an efficient and robust computational technique is needed to analyze the fracture behavior of flexoelectric medium under electro-mechanical loading conditions. Therefore, this work focused on the extension of XIGA formulation and their implementation to predict fracture parameters in the flexoelectric medium. In the present study, the XIGA framework for fracture analysis of piezoelectric materials is enriched by adding flexoelectric physics to it. The model will help to improve the understanding of crack behavior at micro and nano length scales where flexoelectricity dominates over piezoelectricity. The framework can also investigate cracked non-piezoelectric dielectrics that show flexoelectricity at crack tips. The higher-order XIGA formulation was implemented as an in-house developed MATLAB code. The numerical code is tested for mesh independency and further validated by comparing it with existing literature. Several parametric studies have been carried out to investigate how cracks behave for different flexoelectric coefficients under electrical and mechanical loading combinations using electro-mechanical J-integral. Both center and edge crack geometries are investigated for different crack orientations and lengths. Further, a crack interaction study was carried out to understand the behavior of multiple edge cracks.

2. Formulation

2.1. Constitutive Equations and Weak Form

Different approaches can be seen in the past literature to analyze flexoelectric domains computationally.[20,41,48,58,59] We begin our formulation with electric enthalpy density defined in an electromechanical continuum as a function of strain, electric field, and respective gradients.[20] Electric enthalpy density $\mathcal{H}$ in a domain with both flexoelectricity and piezoelectricity can be defined as

$$\mathcal{H}\left(\varepsilon_{ij}, E_i, \varepsilon_{jk,l}, E_{i,j}\right) = \frac{1}{2}\mathbb{C}_{ijkl}\varepsilon_{ij}\varepsilon_{kl} - e_{ikl}E_i\varepsilon_{kl} + d_{ijkl}E_{i,j}\varepsilon_{kl} + f_{ijkl}E_i\varepsilon_{jk,l} - \frac{1}{2}\kappa_{ij}E_iE_j \quad (1)$$

The sum of five terms can be seen on the right-hand side of the equation. The first term on the right-hand side is the elastic strain energy density, defined by fourth-order elastic tensor $\mathbb{C}_{ijkl}$ and strain tensor ε_{ij}. The second term shows the coupling between the electric field E_i and mechanical strain ε_{kl}. Here $E_i = -\phi_{,i}$

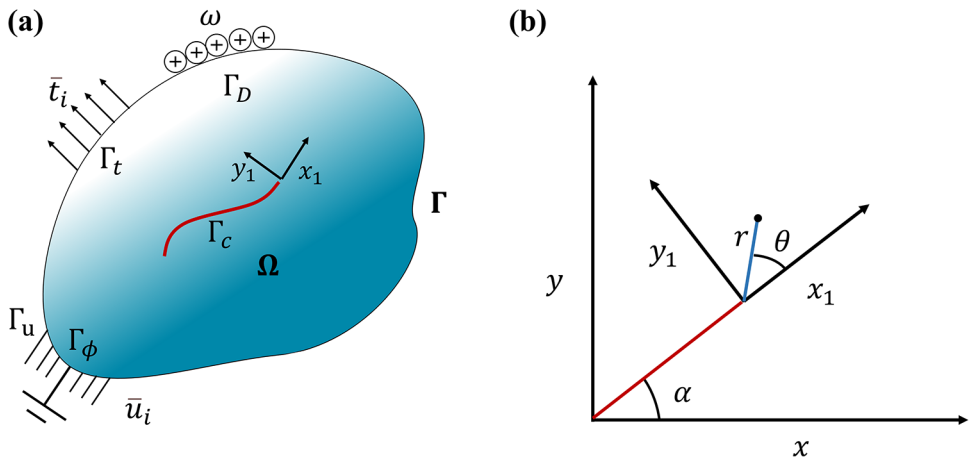

Figure 1. a) The arbitrary domain under consideration with different boundary loads and b) the coordinate system considered in the problem.

where ϕ is the electric potential and e_{ikl} is the third-order piezoelectric tensor. The third and fourth terms show flexoelectric coupling. The fourth-order converse flexoelectric constant d_{ijkl} couples strain ε_{kl} with the electric field gradient $E_{i,j}$. Also, fourth-order direct flexoelectric tensor f_{ijkl} couples electric field E_i with strain gradient $\varepsilon_{jk,l}$. The last term defines electrostatic energy, which has the second-order dielectric tensor κ_{ij} and electric field E_i. A simplified representation of the problem domain with crack is given in **Figure 1**a. The local coordinate axis along the crack and global coordinate axis are shown in Figure 1b. The direct and converse coupling terms in the above expression can be combined into a single term by applying integration by parts and then the Gauss divergence theorem.[20,21,60] This modification will produce a new energy expression with no electric field gradient term. So, the new electric enthalpy density function can also be written using a single flexoelectric material constant μ_{ijkl} as[20]

$$\mathcal{H}\left(\varepsilon_{ij}, E_i, \varepsilon_{jk,l}\right) = \frac{1}{2}\,\mathbb{C}_{ijkl}\varepsilon_{ij}\varepsilon_{kl} - e_{ikl}E_i\varepsilon_{kl} - \mu_{ijkl}E_i\varepsilon_{jk,l} - \frac{1}{2}\kappa_{ij}E_iE_j \quad (2)$$

Where $\mu_{ijkl} = d_{iljk} - f_{ijkl}$; Due to the presence of flexoelectricity along with regular stress $\hat{\sigma}_{ij}$ and electric displacement $\hat{D}_i$, higher-order stress $\tilde{\sigma}_{ijk}$ and electric displacement $\tilde{D}_{ij}$ fields are also present and given as

$$\hat{\sigma}_{ij} = \frac{\partial \mathcal{H}}{\partial \epsilon_{ij}},\ \hat{D}_i = -\frac{\partial \mathcal{H}}{\partial E_i},\ \tilde{\sigma}_{ijk} = \frac{\partial \mathcal{H}}{\partial \epsilon_{ij,k}},\ \tilde{D}_{ij} = \frac{\partial \mathcal{H}}{\partial E_{i,j}} \quad (3)$$

The net stresses σ_{ij} and the electric displacements D_i can be written as

$$\sigma_{ij} = \hat{\sigma}_{ij} - \tilde{\sigma}_{ijk,k} = \mathbb{C}_{ijkl}\,\varepsilon_{kl} - e_{kij}E_k + \mu_{lijk}E_{l,k} \quad (4)$$

$$D_i = \hat{D}_i - \tilde{D}_{ij,j} = e_{ikl}\,\varepsilon_{kl} + \kappa_{ij}E_j + \mu_{lijk}\varepsilon_{jk,l} \quad (5)$$

Dirichlet and Neumann boundary conditions for the electric potential are given as follows

$$\phi = \bar{\phi}\ \text{on}\Gamma_\phi \quad (6)$$

$$D_i\,n_i = -\omega\text{on}\Gamma_D \quad (7)$$

Here $\bar{\phi}$ is the applied potential, and ω is the applied electric charge density; n_i is the normal unit vector; also $\Gamma_\phi \bigcup \Gamma_D = \partial\Omega$ and $\Gamma_\phi \cap \Gamma_D = \emptyset$. Mechanical boundary conditions are given as follows[20,41]

$$u_i = \bar{u}_i\ \text{on}\ \Gamma_u \quad (8)$$

$$t_k = n_j\left(\hat{\sigma}_{jk} - \tilde{\sigma}_{ijk,l}\right) - D_j\left(n_i\tilde{\sigma}_{ijk}\right) - \left(D_p n_p\right)n_i n_j\,\tilde{\sigma}_{ijk} = \bar{t}_k\ \text{on}\Gamma_t \quad (9)$$

$\bar{t}_k$ and $\bar{u}_i$ are values of applied traction and displacement at the respective boundaries. $D_j = \partial_j - n_j D^n$ is the surface gradient operator. $D^n = n_k\,\partial_k$ is the normal gradient operator. $\Gamma_u \bigcup \Gamma_t = \partial\Omega$ and $\Gamma_u \cap \Gamma_t = \emptyset$. Other types of boundary conditions that arise due to strain gradients are given as follows

$$u_{i,j}\,n_j = \bar{\nu}_i\ \text{on}\ \Gamma_\nu,\ n_i n_j\,\tilde{\sigma}_{ijk} = \bar{r}_k\ \text{on}\ \Gamma_r \quad (10)$$

$\bar{\nu}_i$ and $\bar{r}_k$ are the prescribed normal derivative of displacement and higher-order traction, respectively. $u_{i,j}$ is the gradient of displacement field. We ignore these higher-order tractions in the present study and take them as zero. Also here: $\Gamma_\nu \bigcup \Gamma_r = \partial\Omega$ and $\Gamma_\nu \cap \Gamma_r = \emptyset$. Applying the principle of virtual work will result in a weak form as follows[20]

$$\int_\Omega \left(C_{ijkl}\delta\varepsilon_{ij}\varepsilon_{kl} - e_{kij}E_k\delta\varepsilon_{ij} - \mu_{lijk}E_l\delta\varepsilon_{ij,k} - \kappa_{ij}\delta E_iE_j\right)\mathrm{d} - \int_{\Gamma_t}\bar{t}_i\delta u_i\mathrm{d}S + \int_{\Gamma_D}\omega\delta\phi\mathrm{d}S = 0 \quad (11)$$

Here δ is the variational operator. The weak form can be used further for numerical analysis.

2.2. Isogeometric Analysis

2.2.1. NURBS and B-Splines

Parametric curves such as NURBS are widely used to represent different smooth geometries in computer-aided geometric design (CAGD) applications. In splines-based geometric modeling, control points are given as inputs, and curves and surfaces are

approximated using a smooth polynomial basis.[61] For the given $n+1$ control points with non-negative weight w_i and a knot vector containing $m+1$ knots, the NURBS curve of degree p is defined as

$$\boldsymbol{C}\ (t) = \sum_{i=0}^{n} R_{i,p}\ (t)\ \ P_i \tag{12}$$

P_i is control points, t is the parameter that varies from 0 to 1. Here the relation $m = n + p + 1$ is held. The coefficient $R_{i,p}$ is the NURBS basis function and is defined as

$$R_{i,p}\ \ (t) = \frac{N_{i,p}\ (t)\ w_i}{\sum_{j=0}^{n} N_{j,p}\ (t)\ w_j} \tag{13}$$

The B-spline basis functions of degree p, $N_{i,p}(t)$ is defined recursively using the Cox-de Boor recursion formula

$$N_{i,0}\ \ (t) = \begin{cases} 1 \text{ if } t_i \le t \le t_{i+1} \\ \\ 0 \text{ otherwise} \end{cases} \tag{14}$$

$$N_{i,p}\ \ (t) = \frac{t\ -\ t_i}{t_{i+p} - t_i}\ N_{i,p-1}\ (t) + \frac{t_{i+p+1} - t}{t_{i+p+1} - t_{i+1}} N_{i+1,p-1}\ (t) \tag{15}$$

Here $t_i \le t \le t_{i+1}$ is the ith knot span of the curve. The first part of the formula in Equation (15) defines step functions equal to one in knot span and zero everywhere else in the parametric space. It can be seen that NURBS basis functions are rational in t and they have properties such as local support and partition of unity, which are useful in different numerical analysis applications. Also, note that if the degree is p then $p+1$ basis functions will be non-zero on that knot span. B-spline basis functions can be considered special cases of NURBS basis functions. The NURBS basis functions will become B-spline basis functions when weights are equal to one. Increasing the weight will result in a curve being more pulled toward the control points. A NURBS surface is defined as

$$\boldsymbol{P}\ \ (r,s) = \sum_{i=0}^{n_x} \sum_{j=0}^{n_y}\ R_{i,p}\ (r)\ \ R_{j,q}\ (s)\ P_{i,j} \tag{16}$$

Where $\boldsymbol{P} = \{x, y\}$ is the surface and $P_{i,j} = \{x_{ij}, y_{ij}\}$ is the control point. For a surface, there are two-knot vectors, one in r and the other in s. The surface is defined with $n_x + 1$ control points in one direction and $n_y + 1$ in the other direction. Also, p and q are the degrees in each direction. As we move ahead, the term "element" will be used to represent knot spans and surface patches.

2.2.2. Displacement and Voltage Approximations

In IGA, surface patches are treated the same way as elements in finite element analysis. They are mapped to the parent element suitable for Gauss quadrature for integration. In the case of FEA, we needed a single mapping from parent space to physical space, while in IGA, we require one extra mapping from parametric space to parent space. Using IGA approximations, we can evaluate the mechanical displacement and electric voltage field inside a surface patch $[r_i, r_{i+1}) \times (s_i, s_{i+1})$ that has $(p+1) \times (q+1)$ control points associated with it as

$$\boldsymbol{u}\ \ (r,s) = \sum_{i=0}^{n_x} \sum_{j=0}^{n_y} R_{i,j}^{p,q}(r,s)\ \boldsymbol{u}^{i,j} \tag{17}$$

$$\phi\ \ (r,s) = \sum_{i=0}^{n_x} \sum_{j=0}^{n_y} R_{i,j}^{p,q}(r,s)\ \phi^{i,j} \tag{18}$$

Where $\boldsymbol{u} = \{u_x, u_y\}$ are the displacement field, and ϕ is the voltage field, $\boldsymbol{u}^{i,j}$ and $\phi^{i,j}$ are the values of displacements and electric potentials at control points. Also, $n_x = p+1$, $n_y = q+1$ and $R_{i,j}^{p,q}(r,s) = R_{i,p}\ (r) R_{j,q}(s)$.

2.3. Extended Isogeometric Analysis

Using enrichment terms in approximations in a similar way as that of the extended finite element method (XFEM) for elements containing crack faces and crack tips, we get displacement and voltage field as[50,51]

$$\boldsymbol{u}^h\ \ (\mathbf{x}) = \sum_{j=1}^{n_c} R_j\ (\mathbf{X})\ u_j + \sum_{h=1}^{m_s} R_h\ (\mathbf{X})\ [H\ (\mathbf{X}) - H\ (\mathbf{X}_h)]\boldsymbol{a_h} + \sum_{k=1}^{m_t} R_k\ (\mathbf{X}) \left(\sum_{l=1}^{nf} \left[F_l\ (\mathbf{X}) - F_l\ (\mathbf{X}_l) \right] \boldsymbol{b}_k^l \right) \tag{19}$$

$$\phi^h\ \ (\mathrm{X}) = \sum_{j=1}^{n_c} R_j\ (\mathbf{X})\ \phi_j + \sum_{h=1}^{m_s} R_h\ (\mathbf{X})\ \left[H\ (\mathbf{X}) - H\ (\mathbf{X}_h) \right] \alpha_h + \sum_{k=1}^{m_t} R_k\ (\mathbf{X}) \left(\sum_{l=1}^{nf} \left[F_l\ (\mathbf{X}) - F_l\ (\mathbf{X}_l) \right] \beta_k^l \right) \tag{20}$$

Here n_c is the number of control points associated with the element; m_s and m_t are control points associated with elements that have a crack face and crack tip; $H(\mathbf{X})$ is the Heaviside enrichment function and $F_l(\mathbf{X})$ are the crack tip enrichment functions; nf is the number of these crack tip enrichment functions per degree of freedom; $\boldsymbol{a_h}$ $\boldsymbol{b_k^l}$, α_h, and β_k^l are the additional degree of freedom associated with enrichment terms. We used conventional fourfold enrichment functions since they have proven accurate for the electro-mechanical domain.[62] Converting the weak form given in Equation (11) to matrix notations will result in the following equation

$$\{\delta u\}^T \left(\int_{\Omega_e} \left[B_u\right]^T [C] \left[B_u\right] \mathrm{d} \right) \{u\} + \{\delta u\}^T \left(\int_{\Omega_e} \left[B_u\right]^T [e]^T \left[B_\emptyset\right] \mathrm{d} \right) \{\emptyset\} + \{\delta \emptyset\}^T \left(\int_{\Omega_e} \left[B_\emptyset\right]^T [e] \left[B_u\right] \mathrm{d} \right) \{u\} + \{\delta u\}^T \left(\int_{\Omega_e} \left[H_u\right]^T [\mu]^T \left[B_\emptyset\right] \mathrm{d} \right) \{\emptyset\} + \{\delta \emptyset\}^T \left(\int_{\Omega_e} \left[B_\emptyset\right]^T [\mu] \left[H_u\right] \mathrm{d} \right) \{u\}$$

$$-\{\delta\emptyset\}^T\left(\int_{\Omega_e}\left[B_\emptyset\right]^T[e]\left[B_\emptyset\right]\mathrm{d}\right)\{\emptyset\}$$

$$=\{\delta u\}^T\int_{\Gamma_{t_e}}\left[N_u\right]^T\{t\}\mathrm{d}^\circ\mathrm{C}-\{\delta\emptyset\}^T\int_{\Gamma_{D_e}}\left[N_\emptyset\right]^T\{\omega\}\mathrm{d}^\circ\mathrm{C} \quad (21)$$

And the finite element equation is given as follows

$$\begin{bmatrix}K_{uu} & K_{u\emptyset}\\ K_{\emptyset u} & K_{\emptyset\emptyset}\end{bmatrix}\begin{bmatrix}U\\ \emptyset\end{bmatrix}=\begin{bmatrix}f_u\\ f_\emptyset\end{bmatrix} \quad (22)$$

where

$$K_{uu}=\int_{\Omega_e}\left[B_u\right]^T[C]\left[B_u\right]\ \mathrm{d} \quad (23)$$

$$K_{u\emptyset}=\int_{\Omega_e}\left[B_u\right]^T[e]^T\left[B_\emptyset\right]+\left[H_u\right]^T[\mu]^T\left[B_\emptyset\right]\ \mathrm{d} \quad (24)$$

$$K_{\emptyset u}=\int_{\Omega_e}\left[B_\emptyset\right]^T[e]\left[B_u\right]+\left[B_\emptyset\right]^T[\mu]\left[H_u\right]\ \mathrm{d} \quad (25)$$

$$K_{\emptyset\emptyset}=\int_{\Omega_e}\left[B_\emptyset\right]^T[e]\left[B_\emptyset\right]\ \mathrm{d} \quad (26)$$

$$f_u=\int_{\Gamma_{t_e}}\left[R_u\right]^T\{\bar{t}\}\mathrm{d}^\circ\mathrm{C} \quad (27)$$

$$f_\emptyset=\int_{\Gamma_{D_e}}\left[R_\emptyset\right]^T\{\omega\}\mathrm{d}^\circ\mathrm{C} \quad (28)$$

Also here:

$$\left[B_u\right]=\begin{bmatrix}R_{i,x} & 0\\ 0 & R_{i,y}\\ R_{i,y} & R_{i,x}\end{bmatrix} \quad (29)$$

Here $R_{i,x}$ is the first derivatives of the basis functions with x and $R_{i,y}$ is the first derivative of the basis functions with respect to y; also,

$$\left[H_u\right]=\begin{bmatrix}R_{i,xx} & 0\\ 0 & R_{i,yx}\\ R_{i,yx} & R_{i,xx}\\ R_{i,xy} & 0\\ 0 & R_{i,yy}\\ R_{i,yy} & R_{i,xy}\end{bmatrix} \quad (30)$$

$[H_u]$ contains second derivatives of basis functions. Here $R_{i,xx}$ is the second derivative of R_i etc. Also

$$\left[B_\emptyset\right]=\begin{bmatrix}R_{i,x}\\ R_{i,y}\end{bmatrix} \quad (31)$$

To transform the derivatives from physical space to parametric space following steps are carried out

$$\begin{Bmatrix}R_{i,\xi}\\ R_{i,\eta}\end{Bmatrix}=\begin{bmatrix}x_\xi & y_\xi\\ x_\eta & y_\eta\end{bmatrix}\begin{Bmatrix}R_{i,x}\\ R_{i,y}\end{Bmatrix} \quad (32)$$

Here x and y represents the physical space; ξ and η represent parametric space. Also

$$\begin{bmatrix}x_\xi & x_\eta\\ y_\xi & y_\eta\end{bmatrix}=\begin{Bmatrix}x_i\\ y_i\end{Bmatrix}\begin{Bmatrix}R_{i,\xi} & R_{i,\eta}\end{Bmatrix} \quad (33)$$

The higher-order derivatives can be obtained from the following set of equations

$$\begin{bmatrix}(x_{,\xi})^2 & 2x_{,\xi}y_{,\xi} & (y_{,\xi})^2\\ x_{,\xi}x_{,\eta} & y_{,\eta}x_{,\xi}+y_{,\xi}x_{,\eta} & y_{,\xi}y_{,\eta}\\ (x_{,\eta})^2 & 2x_{,\eta}y_{,\eta} & (y_{,\eta})^2\end{bmatrix}\begin{Bmatrix}R_{i,xx}\\ R_{i,xy}\\ R_{i,yy}\end{Bmatrix}=\begin{Bmatrix}R_{i,\xi\xi}\\ R_{i,\xi\eta}\\ R_{i,\eta\eta}\end{Bmatrix}-\begin{bmatrix}x_{\xi\xi} & y_{\xi\xi}\\ x_{\xi\eta} & y_{\xi\eta}\\ x_{\eta\eta} & y_{\eta\eta}\end{bmatrix}\begin{Bmatrix}R_{i,x}\\ R_{i,y}\end{Bmatrix} \quad (34)$$

In Equation (34), $R_{i,xx}$ and $R_{i,\xi\xi}$ represent the second-order derivatives and in the RHS:

$$\begin{bmatrix}x_{\xi\xi} & y_{\xi\xi}\\ x_{\xi\eta} & y_{\xi\eta}\\ x_{\eta\eta} & y_{\eta\eta}\end{bmatrix}=\begin{bmatrix}R_{\xi\xi} & R_{\xi\xi}\\ R_{\xi\eta} & R_{\xi\eta}\\ R_{\eta\eta} & R_{\eta\eta}\end{bmatrix}\begin{bmatrix}x_i & 0\\ 0 & y_i\end{bmatrix} \quad (35)$$

For a material having both piezoelectricity and flexoelectricity, Equations (4) and (5) can be converted into matrix form as

$$\begin{Bmatrix}\boldsymbol{\sigma}\\ \boldsymbol{D}\end{Bmatrix}=\begin{bmatrix}\boldsymbol{C} & -\boldsymbol{e}\\ \boldsymbol{e} & \boldsymbol{\kappa}\end{bmatrix}\begin{Bmatrix}\boldsymbol{\varepsilon}\\ \boldsymbol{E}\end{Bmatrix}+\begin{bmatrix}0 & \boldsymbol{\mu}_E\\ \boldsymbol{\mu}_S & 0\end{bmatrix}\begin{Bmatrix}\nabla\boldsymbol{\varepsilon}\\ \nabla\boldsymbol{E}\end{Bmatrix} \quad (36)$$

Here $\boldsymbol{C}$,$\boldsymbol{e}$, and $\boldsymbol{\kappa}$ are matrices containing elastic piezoelectric and dielectric material constants. $\nabla\boldsymbol{\varepsilon}$ and $\nabla\boldsymbol{E}$ are the gradients of strain and electric field. For Piezoelectric material poled in the y direction, $\boldsymbol{e}$ can be written as:

$$[e]^T=\begin{bmatrix}e_{11} & e_{21}\\ e_{12} & e_{22}\\ e_{15} & e_{25}\end{bmatrix}=\begin{bmatrix}0 & e_{21}\\ 0 & e_{22}\\ e_{15} & 0\end{bmatrix} \quad (37)$$

The dielectric constant matrix is given as

$$[\kappa]=\begin{bmatrix}\kappa_{11} & 0\\ 0 & \kappa_{22}\end{bmatrix} \quad (38)$$

Flexoelectric material constants are given as

$$\left[\mu_S\right]=\begin{bmatrix}\mu_{11} & \mu_{12} & 0 & 0 & 0 & \mu_{44}\\ 0 & 0 & \mu_{44} & \mu_{12} & \mu_{11} & 0\end{bmatrix} \quad (39)$$

$$\left[\mu_E\right]=\begin{bmatrix}\mu_{11} & 0 & 0 & \\ \mu_{12} & 0 & 0 & \mu_{12}\\ 0 & \mu_{44} & \mu_{44} & \mu_{11}\\ & & & 0\end{bmatrix} \quad (40)$$

For modeling flexoelectricity, second-order derivatives of enrichment functions along with first-order derivatives at crack tips are needed. The coordinate axes used in the problem domain containing the crack are shown in Figure 1. Here (x_1, y_1) is the local

coordinates of the crack tip, whereas (x, y) is the global coordinates. (r, θ) are circular coordinates defined about the crack tip as the origin. (x_1, y_1) and (r, θ) are related as follows

$$\tan\theta = \frac{y_1}{x_1} \tag{41}$$

$$r = \sqrt{x_1^2 + y_1^2} \tag{42}$$

And,

$$(x_1, y_1) = (r\cos\theta, r\sin\theta) \tag{43}$$

F_i is the set of four crack tip enrichment functions and their derivatives about (x_1, y_1) is defined as:

$$\frac{\partial F_i}{\partial x_i} = \frac{\partial F_i}{\partial \theta}\frac{\partial \theta}{\partial x_i} + \frac{\partial F_i}{\partial r}\frac{\partial r}{\partial x_i} \tag{45}$$

Their first and second-order derivatives of enrichment functions in r and θ are shown in Appendix A (Table 2). The derivatives of the product of shape functions and enrichment functions are shown below

$$\frac{\partial\left(R\left(F_i - \bar{F}_i\right)\right)}{\partial x} = \frac{\partial R}{\partial x}\left(F_i - \bar{F}_i\right) + R\frac{\partial F_i}{\partial x} \tag{46}$$

$$\frac{\partial\left(R\left(F_i - \bar{F}_i\right)\right)}{\partial y} = \frac{\partial R}{\partial y}\left(F_i - \bar{F}_i\right) + R\frac{\partial F_i}{\partial y} \tag{47}$$

Where

$$\frac{\partial F_i}{\partial x} = \frac{\partial F_i}{\partial x_1}\frac{\partial x_1}{\partial x} + \frac{\partial F_i}{\partial y_1}\frac{\partial y_1}{\partial x} \tag{48}$$

$$\frac{\partial F_i}{\partial y} = \frac{\partial F_i}{\partial x_1}\frac{\partial x_1}{\partial y} + \frac{\partial F_i}{\partial y_1}\frac{\partial y_1}{\partial y} \tag{49}$$

Here F_i is the set of four enrichment functions and $\bar{F}_i$ is the nodal values of the enrichment function. R is the shape function associated with the node. We assume the crack is straight and make an angle α with the global (x, y) coordinate system. The second-order derivatives will be

$$\frac{\partial^2\left(R\left(F_i - \bar{F}_i\right)\right)}{\partial x^2} = \frac{\partial^2 R}{\partial x^2}\left(F_i - \bar{F}_i\right) + \frac{\partial F_i}{\partial x}\frac{\partial R}{\partial x} + \frac{\partial F_i}{\partial x}\frac{\partial R}{\partial x} + R\frac{\partial^2 F_i}{\partial x^2} \tag{50}$$

$$\frac{\partial^2\left(R\left(F_i - \bar{F}_i\right)\right)}{\partial y^2} = \frac{\partial^2 R}{\partial y^2}\left(F_i - \bar{F}_i\right) + \frac{\partial F_i}{\partial y}\frac{\partial R}{\partial y} + \frac{\partial F_i}{\partial y}\frac{\partial R}{\partial y} + R\frac{\partial^2 F_i}{\partial y^2} \tag{51}$$

$$\frac{\partial^2\left(R\left(F_i - \bar{F}_i\right)\right)}{\partial x\partial y} = \frac{\partial^2 R}{\partial x\partial y}\left(F_i - \bar{F}_i\right) + \frac{\partial F_i}{\partial y}\frac{\partial R}{\partial x} + \frac{\partial F_i}{\partial x}\frac{\partial R}{\partial y} + R\frac{\partial^2 F_i}{\partial x\partial y} \tag{52}$$

Where

$$\frac{\partial^2 F_i}{\partial x^2} = \frac{\partial^2 F_i}{\partial x_1^2}\cos^2\alpha - 2\frac{\partial^2 F_i}{\partial x_1 y_1}\cos\alpha\sin\alpha - \frac{\partial^2 F_i}{\partial y_1^2}\sin^2\alpha \tag{53}$$

$$\frac{\partial^2 F_i}{\partial x\gamma^2} = \frac{\partial^2 F_i}{\partial x_1^2}\sin^2\alpha + 2\frac{\partial^2 F_i}{\partial x_1 y_1}\cos\alpha\sin\alpha + \frac{\partial^2 F_i}{\partial y_1^2}\cos^2\alpha \tag{54}$$

$$\frac{\partial^2 F_i}{\partial x\partial y} = \frac{\partial^2 F_i}{\partial x_1^2}\cos\alpha\sin\alpha + \frac{\partial^2 F_i}{\partial x_1 y_1}\cos\alpha\cos\alpha - \frac{\partial^2 F_i}{\partial x_1 y_1}\sin\alpha\sin\alpha - \frac{\partial^2 F_i}{\partial y_1^2}\cos\alpha\sin\alpha \tag{55}$$

2.4. J-Integral

Strains, stresses, electric fields, electric displacement values, and their gradients are obtained as the results of numerical simulation. Using these parameters, we can calculate the energy release rate from the crack tip using a path-independent electro-mechanical J-integral. The integral's path-independent property is related to the crack faces being traction free and electrically impermeable. The line-integral form of J-integral is converted to an area integral suitable for numerical evaluation, which is calculated in the post-processing step of analysis.[52,53,63–65] Higher-order stresses and electric displacements are ignored for the simplicity of the solution. However, they will still include strain and electric field gradients through the electric enthalpy density term to the J-integral. The electro-mechanical J-integral in the area form is given as

$$J = \int_A \left(\sigma_{ij}\frac{\partial u_i}{\partial x_1} + D_j\frac{\partial \phi}{\partial x_1} - \mathcal{H}\delta_{1j}\right)\frac{\partial q}{\partial x_j}\,dA \tag{56}$$

Where $\mathcal{H}$ is given as

$$\mathcal{H} = \frac{1}{2}\mathrm{C}_{ijkl}\epsilon_{ij}\epsilon_{kl} - e_{ikl}E_i\epsilon_{kl} - \mu_{ijkl}E_i\epsilon_{jk,l} - \frac{1}{2}\kappa_{ij}E_iE_j \tag{57}$$

Here u_i is displacement field x_1 is the horizontal coordinate in local coordinate system of the crack. D_j is the electric displacement, ϕ is the electric potential, $\mathcal{H}$ is the strain energy density or enthalpy term. δ_{1j} is the Kronecker delta. q is the weighting function that is defined as a zero inside the path and one outside the path. J-integral can be written in the following form using matrix notations

$$J = \int_A \left(\begin{Bmatrix}\frac{\partial u}{\partial x} & \frac{\partial v}{\partial x}\end{Bmatrix}\begin{bmatrix}\sigma_x & \tau_{xy}\\ \tau_{xy} & \sigma_y\end{bmatrix} - \begin{Bmatrix}\frac{\partial \phi}{\partial x}\end{Bmatrix}\begin{Bmatrix}D_x & D_y\end{Bmatrix} - \mathcal{H}\begin{Bmatrix}1 & 0\end{Bmatrix}\right)\begin{Bmatrix}\frac{\partial q}{\partial x}\\ \frac{\partial q}{\partial y}\end{Bmatrix} \tag{58}$$

Making some rearrangements will result in the following

$$J = \int_A \left(\begin{Bmatrix}\frac{\partial u}{\partial x} & \frac{\partial v}{\partial x}\end{Bmatrix}\begin{bmatrix}\sigma_x & \tau_{xy}\\ \tau_{xy} & \sigma_y\end{bmatrix}\begin{Bmatrix}\frac{\partial q}{\partial x}\\ \frac{\partial q}{\partial y}\end{Bmatrix} - \begin{Bmatrix}\frac{\partial \phi}{\partial x}\end{Bmatrix}\begin{Bmatrix}D_x & D_y\end{Bmatrix}\begin{Bmatrix}\frac{\partial q}{\partial x}\\ \frac{\partial q}{\partial y}\end{Bmatrix} - \mathcal{H}\begin{Bmatrix}\frac{\partial q}{\partial x}\end{Bmatrix}\right) \tag{59}$$

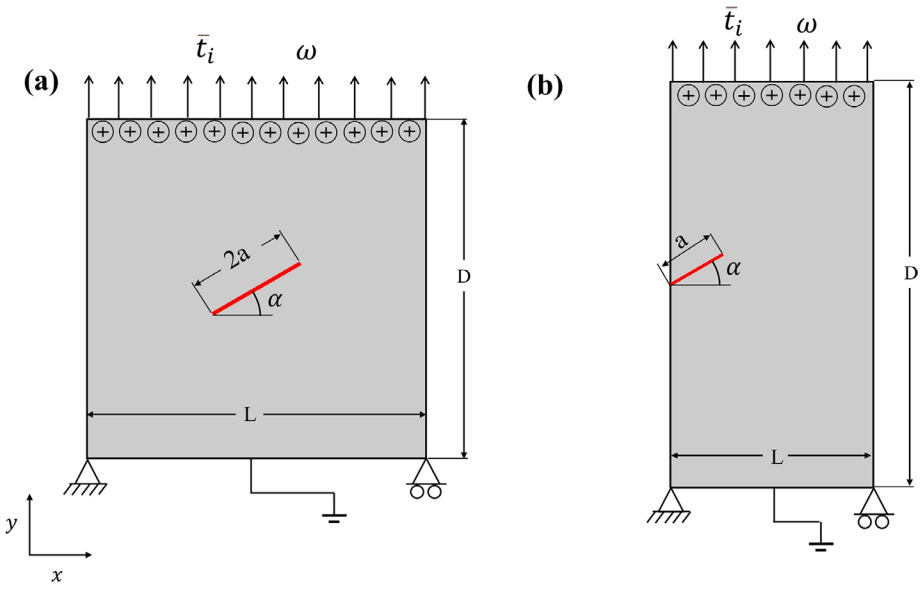

Figure 2. Geometries analyzed in the study are shown. The a) center crack geometry and b) edge crack geometry studied is shown with loading and boundary conditions.

Table 1. Material constants used in the study.

Material properties	Symbol	Values	Reference
Elastic constants	c_{11}	12.6×10^{10} Pa	[55,66]
	c_{13}	5.3×10^{10} Pa	
	c_{33}	11.7×10^{10} Pa	
	c_{55}	3.53×10^{10} Pa	
Piezoelectric material constants	e_{31}	-6.5 C m^{-2}	
	e_{33}	23.3 C m^{-2}	
	e_{15}	17.0 C m^{-2}	
Dielectric constants	κ_{11}	15.1×10^{-9} C^2 N^{-1} m^{-2}	
	κ_{22}	13.0×10^{-9} C^2 N^{-1} m^{-2}	
Flexoelectric coefficient (μ_{12})	μ_{12}	1.0×10^{-6} C m^{-1}	[11]

3. Results and Discussion

3.1. Convergence Study and Validation

Convergence and validation are essential steps before the parametric study to ensure the accuracy of the developed model. The geometries used for the analysis are shown in **Figure 2**a,b. The materials, loading, and boundary conditions are explained in detail in the next section.

3.1.1. Convergence Study

The developed numerical model is investigated for convergence. A convergence study of both primary variables, that is, displacement, and voltage, is performed for both center and edge crack geometries. **Figure 4**a,b shows the displacement variation at the top surface with the number of elements for center and edge

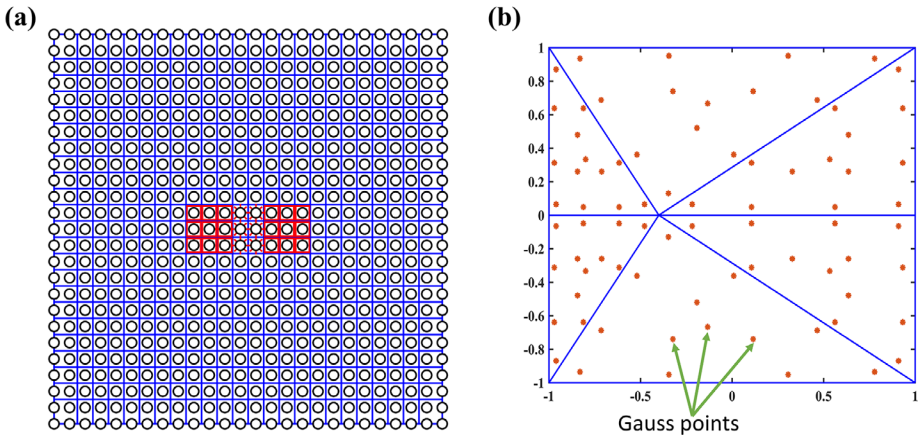

Figure 3. a) Meshed center crack domain with IGA control points and b) Gauss points inside triangulated tip element in parent space.

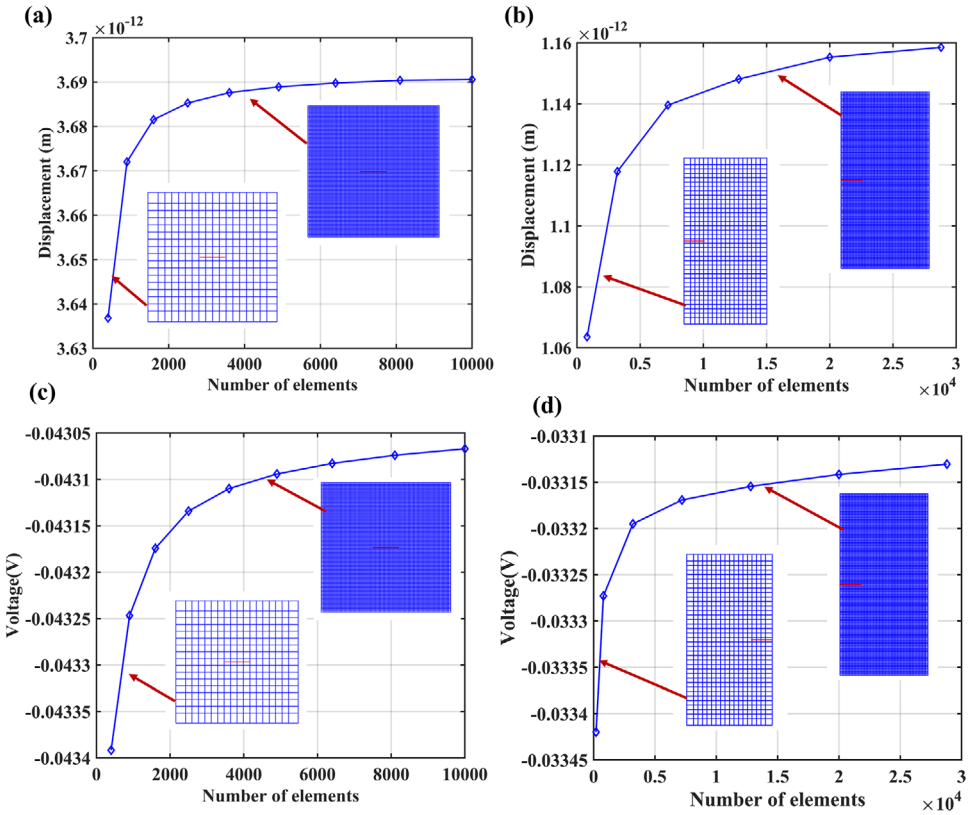

Figure 4. The convergence study for the displacement of a) center crack geometry and b) edge crack geometry; convergence study for voltage of c) center crack geometry and d) edge crack geometry.

crack problems. Figure 4c,d shows the top surface voltage with the number of elements for both center and edge crack domains. It was found that center crack geometry converges ≈10 000 elements and edge crack geometry converges ≈30 000 elements.

3.1.2. Validation

The accuracy of the presented model is ensured by comparing it with previously published works. Due to the unavailability of exactly a similar formulation in IGA, the developed formulation is compared with the gradient elasticity model in the FEM framework conducted by Sladek et al.[55] The same geometry, material, crack orientation, loading, and boundary conditions of the reference study are applied to the XIGA model, and J-integral values are compared. The exact enter crack geometry in the reference paper is used for comparison. The cracks are kept at horizontal positions with a crack length of $a = 1\times10^{-7}$m and $L = D = 10a$ was used. Lead zirconate titanate (PZT) was used as the piezoelectric material, and its piezoelectric and flexoelectric material constants are shown in **Table 1**. Mechanical traction of $\bar{t} = 1.17\times10^{6}$ *Pa* is applied at the top surface. During the comparison, the flexoelectric constant was taken as μ_{12}= 1×10^{-6} C m^{-1}.[11] The reference study used strain gradient size factor q, through which the effect of the scaling parameter was implemented in the formulation. We compared the results obtained when $q = 4$, and found good agreement with the current

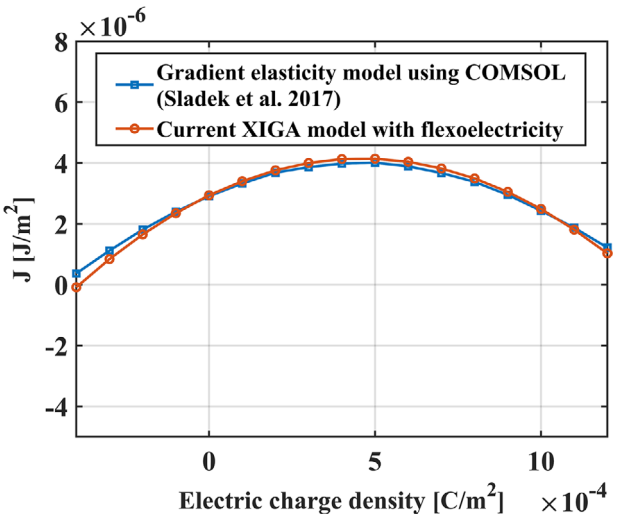

Figure 5. Validation of present XIGA model with flexoelectricity by comparing with previous publication; Sladek et al. 2017.[55]

work. Results are compared in a wide range of electric charge densities varying from −4 to 12 C m^{-2}. The comparison is shown in **Figure 5**. The results produced by the current model are in excellent agreement with that of previous work with minimal deviation. A slight variation was found only at extreme positive and negative charge densities. In the presented work, for accurately

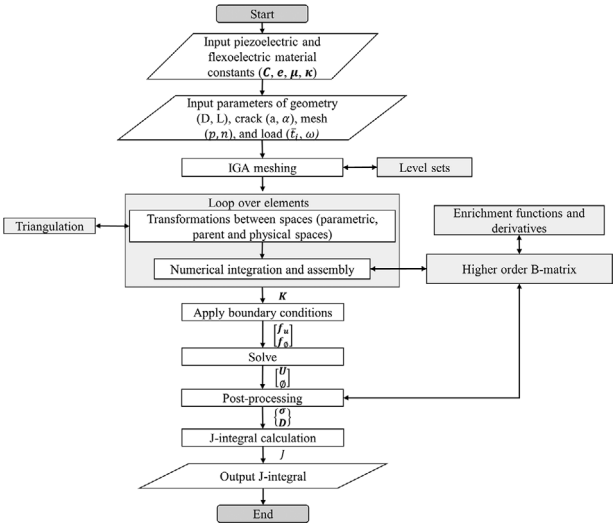

Figure 6. The flowchart of the numerical algorithm proposed for fracture analysis of flexoelectric materials using XIGA.

capturing the fields at the crack tip and along the crack path sub-triangulation technique is employed, while in the literature compared, adaptive meshing was used. The sub-triangulation implemented at the tip element is shown in **Figure 3**b.

3.2. Fields in the Pure Piezoelectric Domain

The present formulation has coupled the piezoelectric and flexoelectric effects together by incorporating the gradient terms in the weak form, as shown in Equation (11). The domain can be converted into pure piezoelectric by giving a value of "zero" to flexoelectric constants. The presented numerical formulation's flexibility allows us to study different problems using a single code, such as pure piezoelectric, pure flexoelectric, and combined flexoelectric-piezoelectric problems. The flowchart for the proposed algorithm is shown in **Figure 6**. XIGA analysis was carried out for pure piezoelectric material, and different electrical and mechanical variable fields such as displacements, voltage, electric displacements, and stresses are plotted. The geometry and loading conditions are shown in Figure 2. The same geometry, material properties, and crack length in Section 3.1.2 are used here also. The material properties of PZT are shown in Table 1. The cracks are kept at horizontal positions with a crack length of $a = 1 \times 10^{-7}$m and $L = D = 10a$ for center crack geometry and, $L = \frac{D}{2} = 5a$ for edge crack geometry was used. Mechanical traction of $\bar{t} = 1.17 \times 10^{6}$ Pa and an electric charge density $\omega = 5 \times 10^{-4}$ C m^{-2} are applied at the top surface. The distribution of important electrostatic and elastic fields, such as stresses, displacements, and electric displacement field components obtained after simulation in the center crack and edge crack domains, are shown in **Figures 7** and **8**. Fields inside a domain with two edge cracks of the same length are shown in **Figure 9**. How

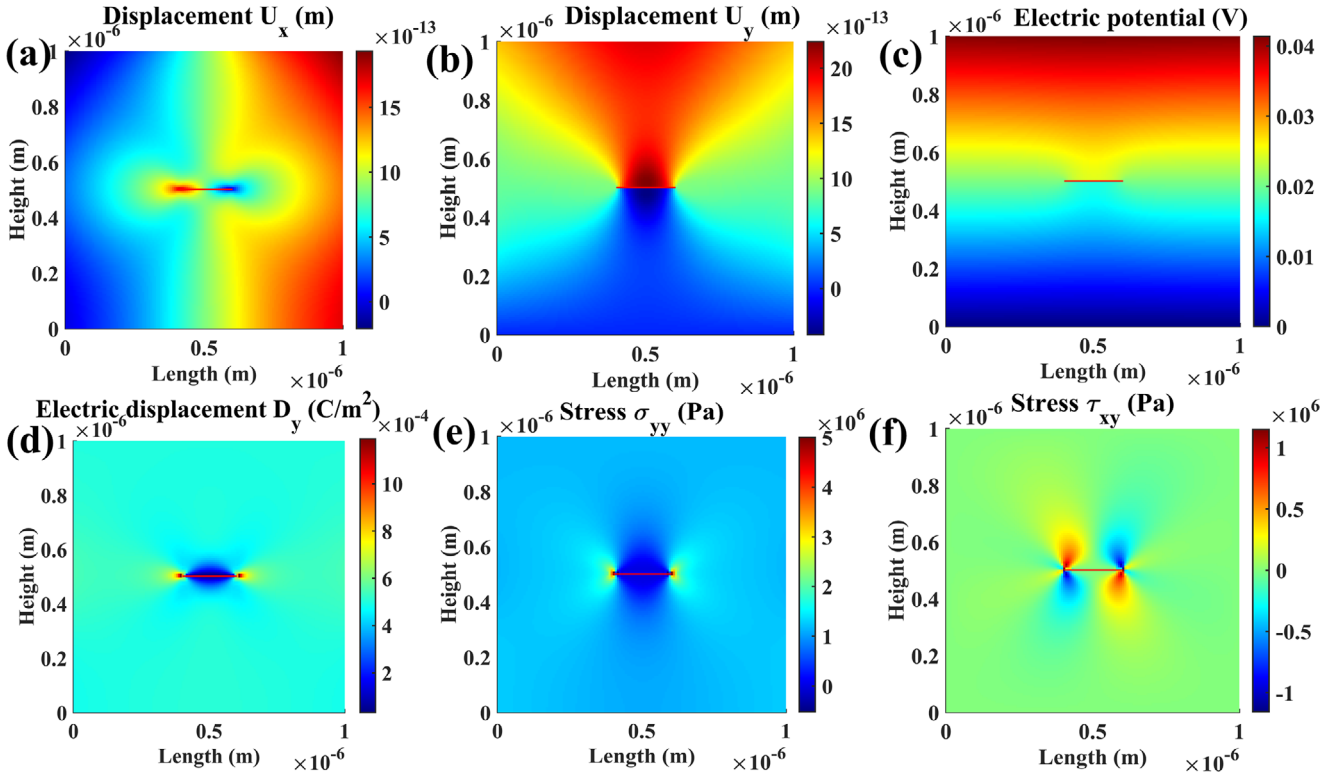

Figure 7. Electrical and mechanical fields in a domain with a center crack under combined electro-mechanical loading are shown: primary variables a) displacement in *x* direction, b) displacement in *y* direction, c) electric potential and secondary variables, d) electric displacement in *y* direction, e) stress in *y* direction, f) shear stress in *x*–*y* plane are shown.

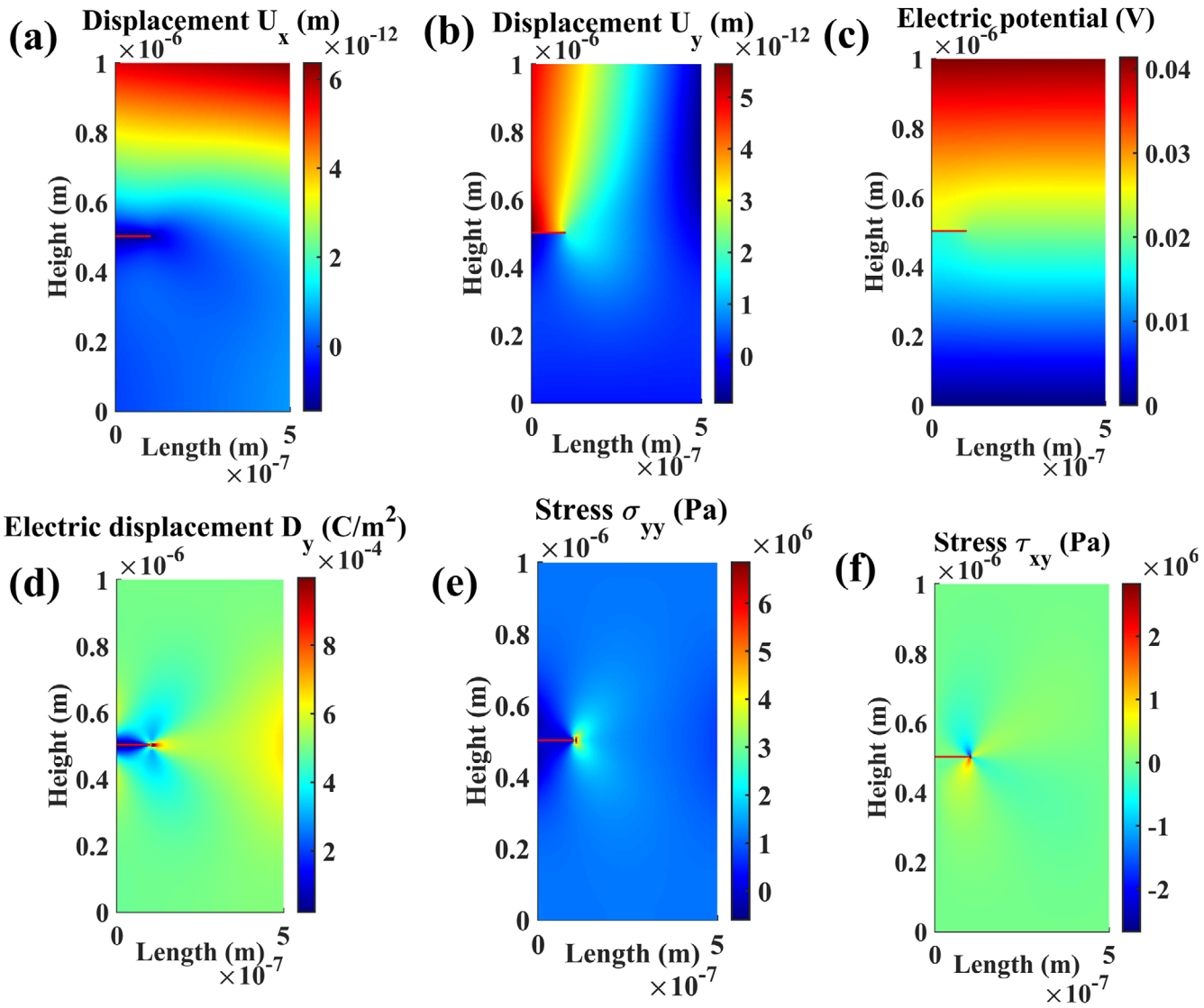

Figure 8. Different fields inside the domain with edge crack: primary variables a) displacement in *x* direction, b) displacement in *y* direction, c) electric potential and secondary variables d) electric displacement in *y* direction, e) stress in *y* direction, f) shear stress in *x*–*y* plane can be seen.

different mechanical and electrical variables interact with the discontinuity and how fields are affected by the presence of a crack in the domain are shown.

3.3. Numerical Studies

A numerical study was conducted in both center and edge crack geometries, considering piezoelectricity and flexoelectricity within the domain. Analysis can be divided into five sections. In the first two analyses, electrical and mechanical loads are varied, and J-integral for different flexoelectric material constants are investigated. In the next three analyses, crack parameters, namely, crack orientation and length, are studied against energy release rate for both center and edge crack geometries with different material constants. The problem geometries used in the numerical analysis, along with loading and boundary conditions, are shown in Figure 2. Standard geometries from the previous publications were used for numerical analysis. For the domain with a center crack of crack length, a, geometric parameters are; $L = D = 1 \times 10^{-6}$ m; $a = 1 \times 10^{-7}$m. For the edge crack domain the crack parameters are; $L = 5 \times 10^{-7}$m; $D = 1 \times 10^{-6}$ m; $a = 1 \times 10^{-7}$m. One of the most utilized piezoelectric materials, lead zirconate titanate (PZT), was used in this analysis. Piezoelectric material properties of PZT are given in Table 1. Material properties were taken from previous publications.[55,66]

Flexoelectric material properties of PZT are given in Table 1. In the parametric study section effect of a range of flexoelectric constants on the fracture behavior of the material was studied. An assumption of plane-strain condition is applied in the study. Important steps in the algorithm and data flow are shown in Figure 6. Poling is assumed in the second direction, that is *y*-

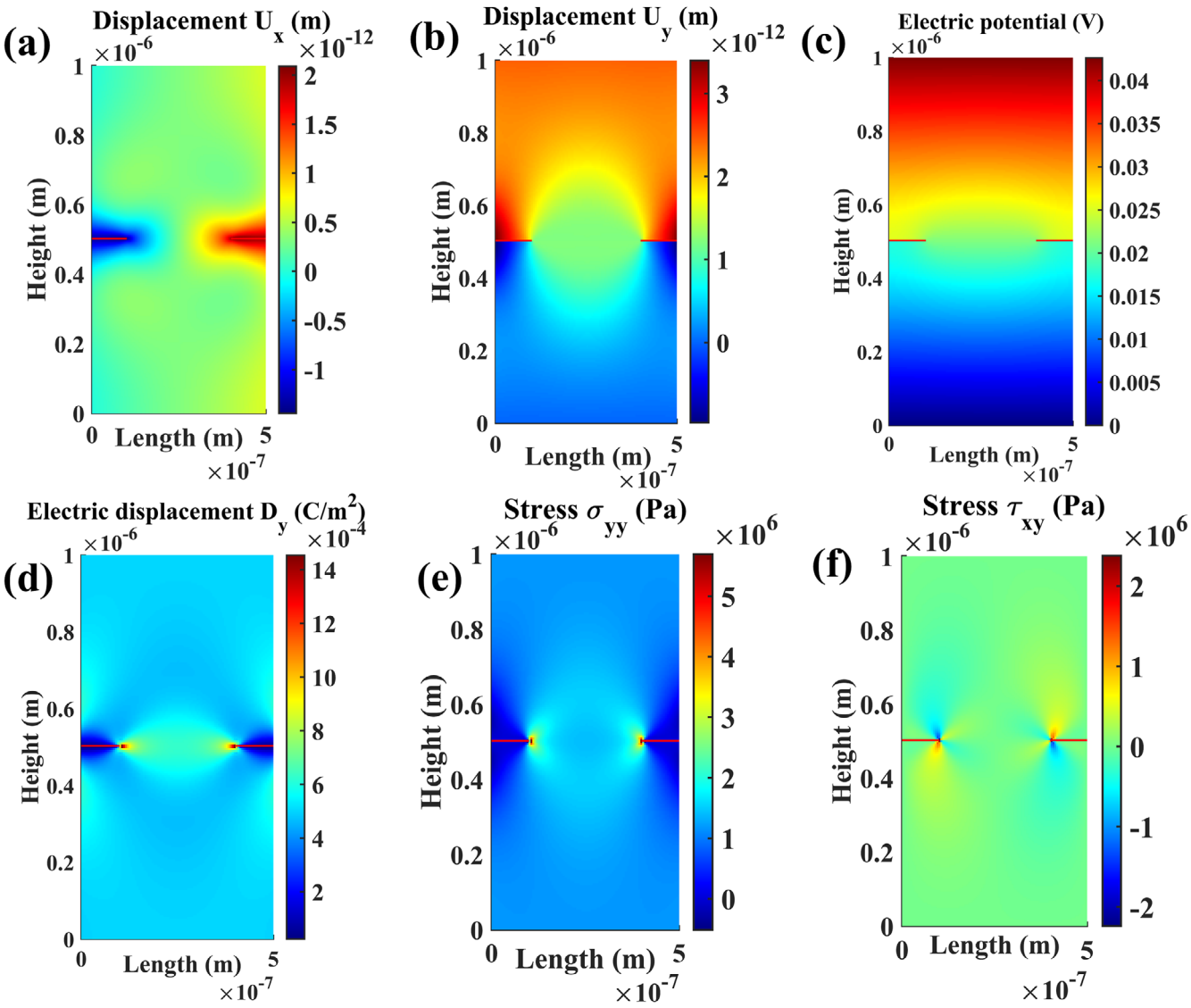

Figure 9. Different electrical and mechanical fields inside a domain have two edge cracks. How fields generated by two cracks interact also can be seen; primary variables a) displacement in the *x* direction, b) displacement in the *y* direction, c) electric potential, and secondary variables d) electric displacement in the *y* direction, e) stress in *y* direction, f) shear stress in the *x*–*y* plane.

direction in the current 2D framework. The domain has meshed with sufficient elements obtained from the convergence study for both geometries. A representation of meshed domain is shown in Figure 3a. Also, in the same figure, split-enriched and tip-enriched control points along the crack can be seen. The Newton–Raphson method was used to numerically obtain the crack tip in a parent element. Triangulation is done in the parent element, and the gauss points are shown in Figure 3b. The problem domain is investigated under combined electrical and mechanical load. Dirichlet–Neumann-type boundary conditions are applied to the problem in both displacement and electric potential fields. The bottom surface is fixed with displacement $\bar{u} = 0$, and earthing is given so that the primary variable $\phi = 0$. The following section presents a parametric analysis where electric and mechanical loading is varied for different material properties and crack geometries, and corresponding fracture behavior is analyzed.

3.3.1. Variation of J-Integral with Electric Charge Density

This section analyzes the fracture behavior of edge and center crack geometries under varying electrical and fixed mechanical loading. A constant, uniformly distributed mechanical traction $\bar{t} = 1.17 \times 10^6$ Pa is applied on the top surface. Electric charge density that varies from -5×10^{-4} to 12×10^{-4} C m^{-2} is also applied along with the constant mechanical load. Analysis was carried out for flexoelectric constants: μ_{12}= 0.5, 0.7, 1.0, 1.5, and 2.0 μC m^{-1}. Variation of J-integral in a central crack geometry is shown in **Figure 10**a, and that of edge crack is shown in Figure 10b. For both center and edge crack geometries, the maximum value of the J-integral can be seen to decrease with the increase of flexoelectric material constant. Also, a shift in the maximum value of J-integral with material constant can be seen. For center crack geometry at μ_{12}= 0.5 μC m^{-1} the maximum value of

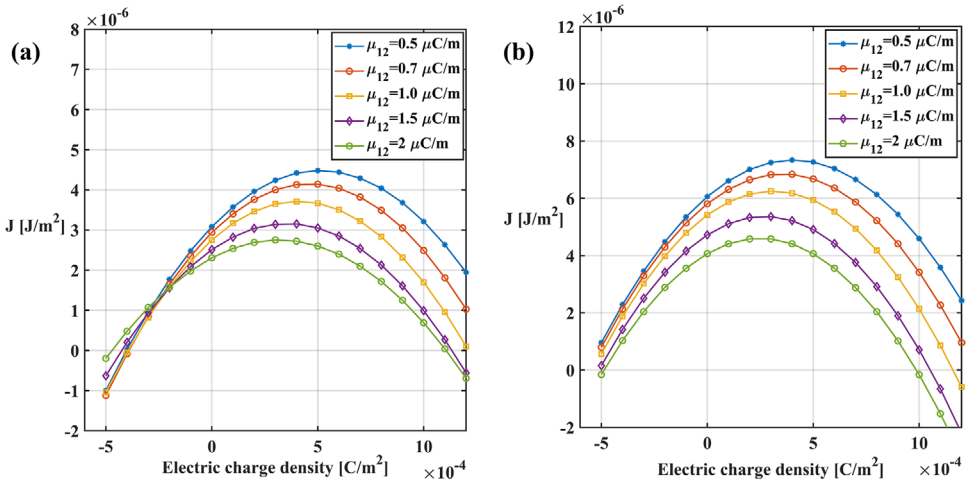

Figure 10. variation of J-integral with applied electric charge density for a) center crack problem and b) edge crack problem.

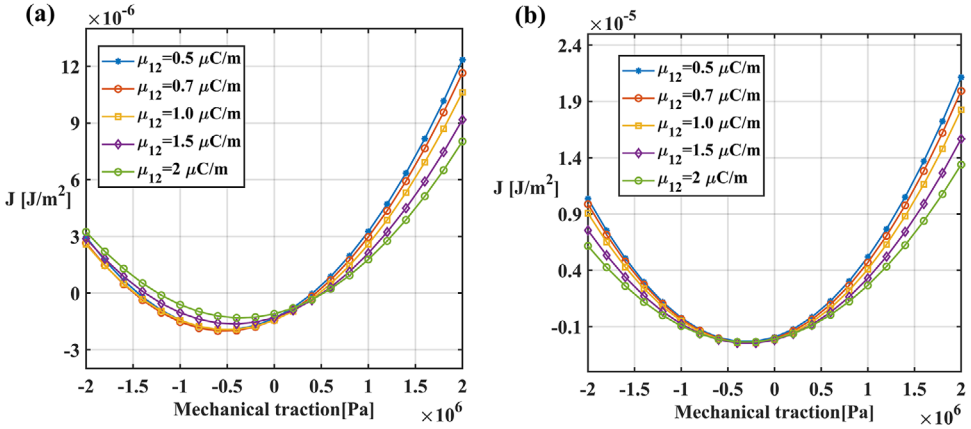

Figure 11. Variation of J integral with mechanical load applied as traction in y direction on the top boundary in a) center crack and b) edge crack.

energy release rate was found to be at 5 C m^{-2} while for μ_{12}= 2 μC m^{-1} the maximum value of energy release rate was found to be at 2 C m^{-2}. In the case of edge crack geometry, shown in Figure 10, a similar trend is observed. When μ_{12}= 0.5 μC m^{-1}, the maximum value of energy release rate 7.2 J m^{-2} occurs at 4 C m^{-2} and reduces to 4.6 J m^{-2} when flexoelectric constant increased to μ_{12}= 2 μC m^{-1}. The reason for reduction in energy release rate around the crack tip can be attributed to the local flexoelectric toughening.[55,57]

3.3.2. Variation of J-Integral with Mechanical Load

The energy release rate from the crack tip is studied against traction load varying from −2 to 2 MPa in y direction for different flexoelectric constants that vary from μ_{12}= 0.5 to 2.0 μC m^{-1}. The electric charge density at the top edge was kept constant as $\omega = 5 \times 10^{-4}$ C m^{-2} throughout this analysis. **Figure 11**a shows the variation of J-integral with mechanical traction load for a center crack geometry, while Figure 11b shows the J-integral variation for edge crack geometry.

Under tension, J-integral increases with load, while under compressive loading, J-integral first reduces and then increases. J-integral can take negative values at a particular load range in both center crack and edge crack geometries. As an example, in the case of center crack geometry for μ_{12} = 1 μC m^{-1}, the J-integral is negative from 0.5 to −1.5 MPa. Beyond this range in positive and negative loading, there is a drastic increase in J-integral. It can also be observed that the energy release rate becomes zero at two particular mechanical loads, one compressive and another tensile, for a constant electric charge density applied at the boundary. It can be seen that changing flexoelectric constants under varying mechanical loads have less effect than that under varying electrical loads. Piezoelectric fracture toughening is known to be negligible under pure mechanical loading, and a similar effect is also visible in a combination of both flexoelectric and piezoelectric domains.[67]

3.3.3. Variation of J-Integral with the Angle of Crack

In this parametric study, we varied the angle of the crack with horizontal, α for both central and edge crack problems. J-integral

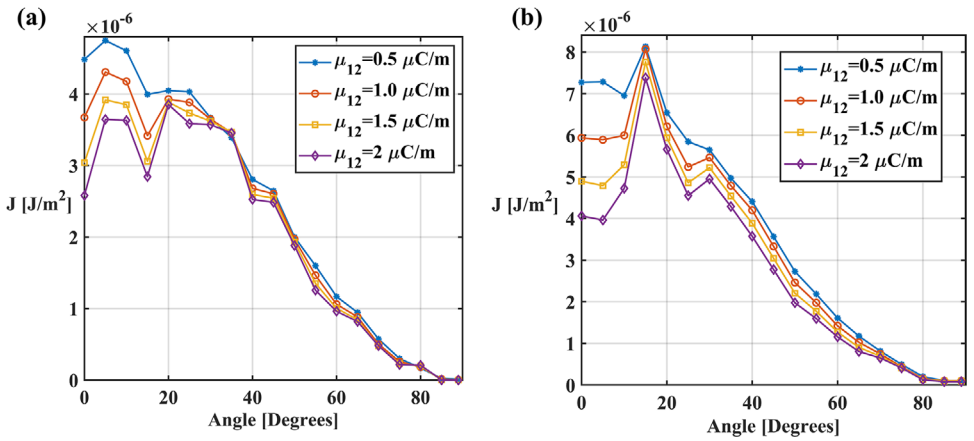

Figure 12. Variation of J integral with the crack angle in a) center crack geometry and b) edge crack geometry.

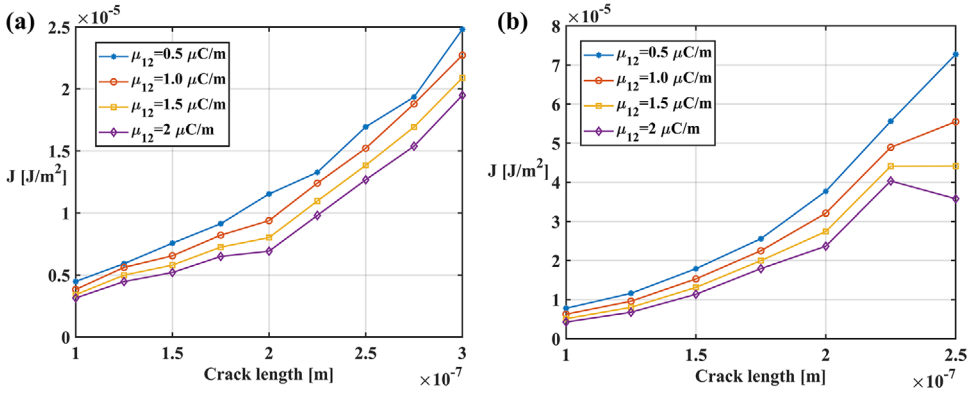

Figure 13. Variation of J-integral with crack length in the a) center crack domain and b) edge crack domain.

was calculated at different angles for different flexoelectric constants. In order to fully understand the impact of crack orientation, the angle of the crack is varied from 0° to 90°, taking into account the problem's symmetry. Mechanical traction and electric charge density was kept fixed as follows: $\bar{t} = 1.17 \times 10^6$ Pa and $\omega = 5 \times 10^{-4}$ C m^{-2}. In this study also, flexoelectric material parameters are varied as follows: μ_{12}= 0.5 to 2.0 μC m^{-1}. **Figure 12**a shows the J-integral analysis for the center crack, and Figure 12b shows the results for the edge crack geometry. It is observed that for both the center crack and edge crack, the J-integral first increases and reaches a maximum value. For the center crack, the maximum value is attained at ≈5°, while for the edge crack, the maximum value is reached at ≈15°. After a slight fluctuation, the J-integral approaches zero at 90°.

3.3.4. Variation of J-Integral with crack length

In this study, J-integral is investigated against crack length. The central crack and edge crack problems are investigated at different flexoelectric material constants, as shown in **Figure 13**a,b. The crack length was varied from 1×10^{-7} to 3×10^{-7}m for center crack and 1×10^{-7} to 2.5×10^{-7}m for edge crack. Mechanical traction and electric charge density was kept constant as follows: $\bar{t} = 1.17 \times 10^6$ Pa and $\omega = 5 \times 10^{-4}$ C m^{-2}. Here also flexoelectric material parameters vary from μ_{12}= 0.5 to 2.0 μC m^{-1}. The drastic increase in the energy release rate with crack length increments along the horizontal direction is seen. For the edge crack (Figure 13b), the J-integral tends to stabilize after a certain crack length which is not observed in the case of the center crack. This behavior is more prominent in the material having a higher flexoelectric constant and can be due to the additional fracture toughening at the crack tip caused by flexoelectricity.

3.3.5. Crack Interaction Study

A domain with two edge cracks has been investigated for the crack interaction study. The edge cracks are placed on the opposite side of the domain, and the crack length on the right side has been increased. The energy release rate from both the crack tips is investigated at different flexoelectric constants. The geometry of the domain is the same as that used in the previous edge crack analysis except for the additional edge crack. The crack length of the left edge crack was increased from 1×10^{-7} to 3×10^{-7}m. The electrical and mechanical loading was kept at constant values of: $\bar{t} = 1.17 \times 10^6$ Pa and $\omega = 5 \times 10^{-4}$ C m^{-2}. The analysis was conducted at different flexoelectric values varying from μ_{12}= 0.5 to 1.5 μC m^{-1}. The domain under analysis and the results are shown in **Figure 14**. J-integral at both crack tips is found to increase with the increment of crack length of the second crack. At the first crack tip, the J-integral increased

Table 2. Derivatives of enrichment functions.

Functions	$F_1 = r^{\frac{1}{2}} \sin\frac{\theta}{2}$	$F_2 = r^{\frac{1}{2}} \cos\frac{\theta}{2}$	$F_3 = r^{\frac{1}{2}} \sin\frac{\theta}{2}\sin\theta$	$F_4 = r^{\frac{1}{2}} \cos\frac{\theta}{2}\sin\theta$
Derivatives				
$\frac{\partial F_i}{\partial x_1}$	$\frac{-r^{-\frac{1}{2}}}{2}\sin\frac{\theta}{2}$	$\frac{r^{-\frac{1}{2}}}{2}\cos\frac{\theta}{2}$	$\frac{-r^{-\frac{1}{2}}}{2}\sin\frac{3\theta}{2}\sin\theta$	$\frac{-r^{-\frac{1}{2}}}{2}\cos\frac{3\theta}{2}\sin\theta$
$\frac{\partial F_i}{\partial y_1}$	$\frac{r^{-\frac{1}{2}}}{2}\cos\frac{\theta}{2}$	$\frac{r^{-\frac{1}{2}}}{2}\sin\frac{\theta}{2}$	$\frac{-r^{-\frac{1}{2}}}{2}(\sin 2\theta + \sin\frac{3\theta}{2}\cos\theta)$	$\frac{r^{-\frac{1}{2}}}{2}(\cos\frac{\theta}{2} + \cos\frac{3\theta}{2}\cos\theta)$
$\frac{\partial^2 F_i}{\partial x_1^2}$	$\frac{r^{-\frac{3}{2}}}{4}\sin\frac{3\theta}{2}$	$\frac{-r^{-\frac{3}{2}}}{4}\cos\frac{3\theta}{2}$	$\frac{3r^{-\frac{3}{2}}}{4}\sin\theta\sin\frac{5\theta}{2}$	$\frac{3r^{-\frac{3}{2}}}{4}\sin\theta\cos\frac{5\theta}{2}$
$\frac{\partial^2 F_i}{\partial x_1 \partial y_1}$	$\frac{-r^{-\frac{3}{2}}}{4}\cos\frac{3\theta}{2}$	$\frac{-r^{-\frac{3}{2}}}{4}\sin\frac{3\theta}{2}$	$\frac{-r^{-\frac{3}{2}}}{4}(\sin\theta\sin\frac{5\theta}{2} + \sin\frac{7\theta}{2})$	$\frac{-r^{-\frac{3}{2}}}{4}(\cos\theta\cos\frac{5\theta}{2} + \cos\frac{7\theta}{2})$
$\frac{\partial^2 F_i}{\partial y_1^2}$	$\frac{-r^{-\frac{3}{2}}}{4}\sin\frac{3\theta}{2}$	$\frac{r^{-\frac{3}{2}}}{4}\cos\frac{3\theta}{2}$	$\frac{r^{-\frac{3}{2}}}{4}(3\cos\theta\cos\frac{5\theta}{2} + \cos\frac{3\theta}{2})$	$\frac{-r^{-\frac{3}{2}}}{4}(3\cos\theta\sin\frac{5\theta}{2} + \sin\frac{3\theta}{2})$

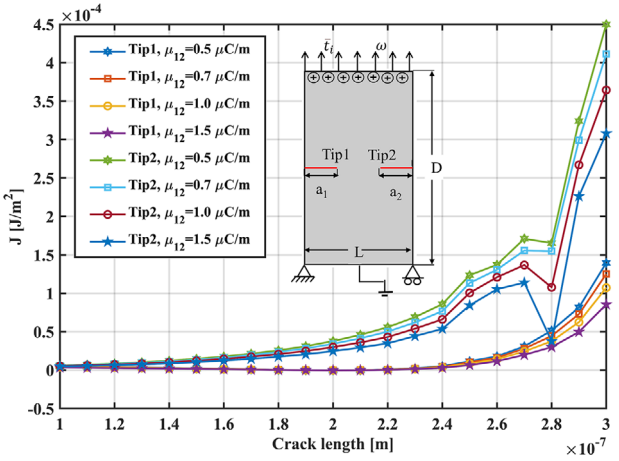

Figure 14. The J-integral values of two edge crack tips on the opposite sides are shown. The domain is shown with the loading and two edge crack tips .

smoothly, while at the second tip, it fluctuated, indicating toughening.

4. Conclusion

Crack analysis of a 2D domain with both piezoelectricity and flexoelectricity has been carried out using XIGA. NURBS-based extended isogeometric analysis helps to capture the gradient terms associated with flexoelectricity. A second-order NURBS basis is used for analysis, which is sufficient to model gradients of strain and electric field. A MATLAB code capable of investigating both flexoelectric and piezoelectric domains individually and in a coupled manner was developed based on the formulation. The numerical model was validated using previous work and found accurate. A convergence study was also conducted to ensure the performance of the code developed. Electro-mechanical J-integral was analyzed by applying a wide range of electrical and mechanical loading. J-integral was also examined in relation to several crack parameters, including crack length and angle. Two geometries with a center crack and an edge crack were investigated. Parametric studies were conducted in a broad range of flexoelectric coefficients, varying from μ_{12}= 0.5 to 2.0 μC m^{-1}.

The analysis has led to the following conclusions:

- It was found that flexoelectric material constants greatly influence the energy release rate from the crack tip and the crack's tendency to extend further under the influence of electric charge density applied at the boundary.
- It is observed that the flexoelectric effect plays a significant role in crack behavior due to strong gradients surrounding the crack tip. This behavior was found to increase with the increase of the flexoelectric constant.
- A reduction in the peak value of J-integral or a toughening phenomenon was observed with an increase in flexoelectricity. This phenomenon was more prominent under varying electric loads than in varying mechanical load conditions.
- It is also observed that J-integral becomes zero at lower electric charge densities as with increasing flexoelectricity. This indicates a possibility of controlling the crack growth by applying suitable electric loads at boundaries.
- Since flexoelectricity is a more general phenomenon in dielectrics, these observations can be further investigated for applications such as structural health monitoring (SHM).

Appendix A

Table 2

Acknowledgements

Authers would like to thank Smart Materials and Stuctures lab, IIT Mandi for providing computational facilities for this research. This research received no specific grant from any funding agency in the public, commercial, or not-for-profit sectors

Conflict of Interest

The authors declare no conflict of interest.

Data Availability Statement

The data that support the findings of this study are available from the corresponding author upon reasonable request.

Keywords

flexoelectricity, fracture mechanics, isogeometric analysis, piezoelectricity, XIGA

Received: November 17, 2022
Revised: January 20, 2023
Published online:

[1] V. K. Varadan, V. V. Varadan, *Smart Mater. Struct.* **2000**, *9*, 953.
[2] R. Bogue, *Assem. Autom.* **2012**, *32*, 3.
[3] S. Tadigadapa, K. Mateti, *Meas. Sci. Technol.* **2009**, *20*, 092001.
[4] S. Saadon, O. Sidek, *Energy Convers. Manag.* **2011**, *52*, 500.
[5] S. Sharma, R. Kiran, P. Azad, R. Vaish, *Energy Convers. Manag.* **2022**, *254*, 115272.
[6] J. F. Tressler, S. Alkoy, R. E. Newnham, *J. Electroceram.* **1998**, *24*, 257.
[7] N. D. Sharma, R. Maranganti, P. Sharma, *J. Mech. Phys. Solids* **2007**, *55*, 2328.
[8] P. V. Yudin, A. K. Tagantsev, *Nanotechnology* **2013**, *24*, 432001.
[9] P. Zubko, G. Catalan, A. K. Tagantsev, *Annu. Rev. Mater. Res.* **2013**, *43*, 387.
[10] B. Wang, Y. Gu, S. Zhang, L. Q. Chen, *Prog. Mater. Sci.* **2019**, *106*, 100570.
[11] L. Shu, R. Liang, Z. Rao, L. Fei, S. Ke, Y. Wang, *J. Adv. Ceram.* **2019**, *8*, 153.
[12] V. S. Mashkevich, K. B. Tolpygo, *Sov. Phys. JETP.* **1957**, *5*, 435.
[13] R. D. Mindlin, *Int. J. Solids Struct.* **1968**, *4*, 637.
[14] X. Jiang, W. Huang, S. Zhang, *Nano Energy* **2013**, *2*, 1079.
[15] U. K. Bhaskar, N. Banerjee, A. Abdollahi, Z. Wang, D. G. Schlom, G. Rijnders, G. Catalan, *Nat. Nanotechnol.* **2015**, *113*, 263.
[16] S. Zhang, K. Liu, M. Xu, S. Shen, *Appl. Phys. Lett.* **2017**, *111*, 082904.
[17] B. Wang, S. Yang, P. Sharma, *Phys. Rev. B* **2019**, *100*, 035438.
[18] J. K. Han, D. H. Jeon, S. Y. Cho, S. W. Kang, S. A. Yang, S. D. Bu, S. Myung, J. Lim, M. Choi, M. Lee, M. K. Lee, *Sci. Rep.* **2016**,*6*, 289562.
[19] S. B. Choi, G. W. Kim, *J. Phys. D: Appl. Phys.* **2017**, *50*, 075502.
[20] A. Abdollahi, C. Peco, D. Millán, M. Arroyo, I. Arias, *J. Appl. Phys.* **2014**, *116*, 093502.
[21] S. Sharma, R. Kumar, M. Talha, R. Vaish, *Adv. Theory Simul.* **2021**, *4*, 2000158.
[22] J. Yang, *Int. J. Fract.* **2004**, *127*, L111.
[23] J. S. Yang, H. G. Zhou, J. Y. Li, J. S. Yang, H. G. Zhou, J. Y. Li, *RSPSA* **2006**, *462*, 3511.
[24] X. Tian, M. Xu, H. Zhou, Q. Deng, Q. Li, J. Sladek, V. Sladek, *J. Appl. Mech.* **2022**, *89*, 041006.
[25] S. Mao, P. K. Purohit, *J. Mech. Phys. Solids* **2015**, *84*, 95.
[26] V. F. Petrenko, R. W. Whitworth, *Physics of Ice*, Oxford University Press, Oxford **2002**.
[27] F. Vasquez-Sancho, A. Abdollahi, D. Damjanovic, G. Catalan, *Adv. Mater.* **2018**, *30*, 1705316.
[28] R. Núñez-Toldrà, F. Vasquez-Sancho, N. Barroca, G. Catalan, *Sci. Rep.* **2020**, *10*, 254.
[29] Z. Suo, C. M. Kuo, D. M. Barnett, J. R. Willis, *J. Mech. Phys. Solids* **1992**, *40*, 739.
[30] M. Kuna, *Arch. Appl. Mech.* **2006**, *76*, 725.
[31] M. Kuna, *Eng. Fract. Mech.* **2010**, *77*, 309.
[32] S. Zhu, H. Liu, *J. Intell. Mater. Syst. Struct.* **2021**, *32*, 1662.
[33] E. Béchet, M. Scherzer, M. Kuna, *Int. J. Numer. Methods Eng.* **2009**, *77*, 1535.
[34] S. K. Singh, I. V. Singh, *Eng. Fract. Mech.* **2020**, *230*, 107015.
[35] H. Pathak, *Mech. Adv. Mater. Struct.* **2020**, *27*, 903.
[36] J. Jena, S. K. Singh, V. Gaur, I. V. Singh, S. Natarajan, *Eng. Fract. Mech.* **2021**, *253*, 107874.
[37] S. Zhu, H. Yu, X. Wu, C. Huang, M. Zhao, L. Guo, *Eng. Fract. Mech.* **2021**, *258*, 108084.
[38] S. Zhu, H. Yu, L. Hao, Z. Shen, J. Wang, L. Guo, *Eur. J. Mech. A. Solids* **2023**, *98*, 104871.
[39] S. Zhu, H. Yu, X. Wu, L. Hao, Z. Shen, J. Wang, L. Guo, *Theor. Appl. Fract. Mech.* **2022**, *122*, 103614.
[40] S. Zhu, H. Yu, L. Hao, B. Wang, Y. Yang, K. Huang, Z. Li, L. Guo, *Compos. Struct.* **2023**, *305*, 116497.
[41] X. Zhuang, B. H. Nguyen, S. S. Nanthakumar, T. Q. Tran, N. Alajlan, T. Rabczuk, *Energies* **2020**, *13*, 1326.
[42] V. P. Nguyen, C. Anitescu, S. P. A. Bordas, T. Rabczuk, *Math Comput. Simul.* **2015**, *117*, 89.
[43] R. Maranganti, N. D. Sharma, P. Sharma, *Phys. Rev. B: Condens. Matter* **2006**, *74*, 014110.
[44] H. Ghasemi, H. S. Park, T. Rabczuk, *Comput. Methods Appl. Mech. Eng.* **2017**, *313*, 239.
[45] T. Q. Thai, T. Rabczuk, X. Zhuang, *Comput. Methods Appl. Mech. Eng.* **2018**, *341*, 718.
[46] B. H. Nguyen, X. Zhuang, T. Rabczuk, *Comput. Struct.* **2018**, *208*, 75.
[47] S. Sharma, R. Kumar, R. Vaish, *Int. J. Smart Nano Mater.* **2021**, *12*, 107.
[48] S. Sharma, A. Kumar, R. Kumar, M. Talha, R. Vaish, *Mech. Mater.* **2020**, *148*, 103456.
[49] J. Yvonnet, L. P. Liu, *Comput. Methods Appl. Mech. Eng.* **2017**, *313*, 450.
[50] S. S. Ghorashi, N. Valizadeh, S. Mohammadi, *Int. J. Numer. Methods Eng.* **2012**, *89*, 1069.
[51] T. Q. Bui, *Comput. Methods Appl. Mech. Eng.* **2015**, *295*, 470.
[52] S. B. Park, C. T. Sun, *Int. J. Fract.* **1993**, *70*, 203.
[53] M. Abendroth, U. Groh, M. Kuna, A. Ricoeur, *Int. J. Fract.* **2002**, *114*, 359.
[54] A. R. Khoei, *Extended Finite Element Method, Theory and Applications*, Wiley, Chichester **2015**.
[55] J. Sladek, V. Sladek, P. Stanak, C. Zhang, C. -L. Tan, *Int. J. Solids Struct.* **2017**, *114*, 1.
[56] J. Sladek, V. Sladek, M. Wünsche, C. Zhang, *Eur. J. Mech. A Solids* **2018**, *71*, 187.
[57] A. Abdollahi, C. Peco, D. Millán, M. Arroyo, G. Catalan, I. Arias, *Phys. Rev. B: Condens. Matter* **2015**, *92*, 25.
[58] A. Abdollahi, D. Millán, C. Peco, M. Arroyo, I. Arias, *Phys. Rev. B: Condens. Matter* **2015**, *91*, 104103.
[59] S. Hu, S. Shen, *Sci. China Phys., Mech. Astron.* **2010**, *538*, 1497.
[60] N. D. Sharma, C. M. Landis, P. Sharma, *J. Appl. Phys.* **2010**, *108*, 024304.
[61] L. Piegl, W. Tiller, *The NURBS Book*, Springer, Berlin, Heidelberg **1995**.
[62] E. Béchet, M. Scherzer, M. Kuna, *Int. J. Numer. Methods Eng.* **2009**, *77*, 1535.
[63] C. F. Gao, M. Zhao, P. Tong, T. Y. Zhang, *Int. J. Eng. Sci.* **2004**, *42*, 2175.
[64] E. Béchet, M. Scherzer, M. Kuna, *Eur. J. Comput. Mech.* **2008**, *17*, 637.
[65] X. Tian, Q. Li, Q. Deng, *Int. J. Fract* **2019**, *215*, 67.
[66] R. Mishra, R. G. Burela, H. Pathak, *Crack Interaction Study in Piezoelectric Materials Under Thermo-Electro-Mechanical Loading Environment*, Springer, Dordrecht **2019**.
[67] R. K. N. D. Rajapakse, X. Zeng, *Acta Mater.* **2001**, *49*, 877.